Investigation of Magnetic Electrodes in Conducting Polymeric Materials: Electrochemical Properties of a Fullerene[C$_{60}$]-Pd Polymer and Iron Oxide Magnetic Nanocomposite

Monika Wysocka-Zolopa,* Kazimierz Wojtulewski, Anna Basa, Dariusz M. Satuła, Karolina H. Markiewicz, Emilia Grądzka, and Krzysztof Winkler*

A composite of iron oxide magnetic nanoparticles and coordination fullerene polymer (C$_{60}$Pd$_3$)$_n$ is formed by chemical deposition of spherical polymer nanoparticles on iron oxide magnetic nanoparticles in benzene containing C$_{60}$ and Pd(0) complex. The composition of the composite can be controlled by the amount of magnetite and concentration of polymerization precursors as well as the time of polymerization. The magnetic composite material Fe$_3$O$_4$-γFe$_2$O$_3$/(C$_{60}$Pd$_3$)$_n$ is used as a model system to investigate its deposition on a magnetic electrode and its electrochemical properties. The iron oxide magnetic nanoparticles ensure both the magnetic activity of the composite and its nanostructured morphology. Both of these factors are responsible for the enhancement of the electrochemical activity of the polymer phase forming the composite in comparison to the pure polymer material deposited on the same magnetic electrode. In the magnetic field of the electrode, the composite undergoes permanent and strong bonding with the surface of the electrode. The nanostructured morphology of the Fe$_3$O$_4$-γFe$_2$O$_3$/(C$_{60}$Pd$_3$)$_n$ composite also provides very good capacitive properties.

1. Introduction

Many applications of inorganic, organic, and organometallic materials as well as hybrid systems require knowledge of their electrochemical properties. They are particularly important for applications in solar cells, electrocatalysis, electrochemical bio(sensors), or electrical energy storage systems. Studies of the electrochemical properties of materials in the solid phase usually require their deposition on the electrode surface. The electrochemical method seems to be the best for the formation of thin solid layers on the electrodes.[1-5] It allows to obtain homogeneous and mechanically durable layers. However, the electrochemical method is limited to materials that can be produced in electro-oxidation or electro-reduction processes. The amount of material deposited on the surface is also limited. The method of solid phase formation on conductive surfaces from a drop of solution or suspension is much more universal.[6-10] Layers created in this way are characterized by high heterogeneity and low mechanical durability. Additionally, the reproducibility of solid layer formation is very low. These parameters can be improved using the spin coating method.[11,12] However, in this case, the mechanical stability of solid films is also a serious problem in research. Charged colloidal nanoparticles can also be deposited on conducting substrates by electrophoretic procedures.[13-17] To better control the solid layer deposition process, the surfaces of the electrodes are often modified accordingly, increasing the adhesion of the studied material to the substrate.[18-21]

The electrochemical properties of electroactive materials can be altered by their incorporation into composites.[22–27] The modification of the morphology, structure, and energy of interaction between composite components is responsible for the changes in these redox properties. Nanoparticle components are particularly useful in creating electrochemically active composites that exhibit nanostructured morphology.

Over the past two decades, magnetite nanoparticles have gained significant interest due to their novel properties and potential for various nanotechnological applications.[28–35] Other advantageous features of these magnetic iron oxide nanoparticles include superparamagnetism, high saturation field, blocking temperature, chemical stability, biocompatibility, and low cost.[36–38] The properties of magnetite nanoparticles depend on the size of the particles and method of preparation. Magnetite

M. Wysocka-Zolopa, K. Wojtulewski, A. Basa, K. H. Markiewicz,
E. Grądzka, K. Winkler
Department of Chemistry
University of Bialystok
Ciolkowskiego 1K, 15–245, Bialystok Poland
E-mail: monia@uwb.edu.pl; winkler@uwb.edu.pl
D. M. Satuła
Department of Physics
University of Bialystok
Ciolkowskiego 1L, 15–245, Bialystok Poland

M = Pd, Pt, Ir, Rh, Au, Ag
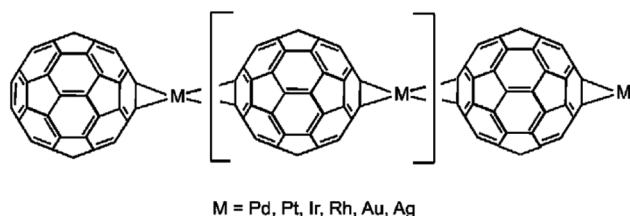
Scheme 1. 1-D chain structure of the fullerene coordination polymer.

can be easily converted into maghemite.[39] This process is facilitated by the increased drying temperature of Fe_3O_4 and the well-developed surface resulting from the nanoparticle nature of the material.

Iron oxide magnetic nanoparticles can also be incorporated into conducting polymer structures to form core–shell morphologies, bulk materials with incorporated magnetite nanoparticles, or heterogeneous mixtures containing nanoparticles of both components.[40–44] The formed composite material exhibits both high conductivity and high magnetic susceptibility. It is also electrochemically active due to conductive polymer-involved electrode processes. They can be used in different applications, such as electrical and magnetic shielding, nonlinear optics, magnetic electrocatalysis, electroactive materials in charge storage devices, and microwave absorbers.[40,43,45–51] To date, research on composites has mainly focused on p-type organic conductive polymers, such as polyaniline,[45,51–54] polypyrrole,[55–58] and polythiophene.[59–61] These polymers show both p and n activity, but their electrochemical properties related to oxidation processes are mostly used in studies and practical applications. These composites are electroactive at positive potentials. Oxidation of the polymeric phase results in the formation of polaron charge carriers. This positive charge is delocalized within a few monomer units due to the conjugation of the π orbitals and provides conductive properties to the material.

Fullerenes are good electron acceptors.[62–64] Incorporation of these carbon spheres into a polymeric matrix leads to the formation of macromolecular systems with reducing properties and a tendency toward n-type doping.[65–71] Metal atoms or metal complexes are coordinated directly to the fullerene cage in an η^2 fashion in coordination fullerene polymers.[68–72] The chain structure of such coordination fullerene polymers is shown in **Scheme 1**. These systems can be formed electrochemically by reduction carried out in solution containing fullerene and transition metal complexes or chemically in solution containing fullerene and low-valence transition metal complexes.[70]

A polymer in which fullerene networks are linked via palladium atoms $(C_{60}Pd_x)_n$ has been particularly well investigated.[73–80] The polymer is formed in a benzene solution containing fullerene[C_{60}] and a complex of Pd(0).[73,80] The structure of the polymeric network depends on the molecular ratio of polymerization precursors in the grown solution, in which 1-D, 2-D, and 3-D polymeric structures can be formed.[73] In the presence of excess palladium complexes, the polymeric material is doped with nanoparticles of metallic palladium.[73,77] The polymer exhibits reversible redox properties related to the reduction of the fullerene cage. In this case, the process of charge transport through the polymeric chain can be described by the "hopping" model.[81,82] Despite the difference in the mechanism of charge transfer in organic polymers with a conjugated π bonds system and coordination fullerene polymers, the shape of voltammetric curves in both systems is similar. The voltammogram peaks in the potential range of fullerene moiety reduction are relatively broad due to the high contribution of the capacity current component. Under cyclic polarization conditions, the fullerene-involved anode and cathode currents are mirror images.

The $(C_{60}Pd_x)_n$ polymer is also incorporated into networks of carbon nanostructures to form composite materials.[10,83–86] Carbon nanostructures significantly improve the mechanical stability and electrochemical performance of polymeric components. They can participate in charge transfer and charge storage processes.[10,86] The porous network of the carbon component enables more effective ion transport in the electrode processes.

In this work, we investigated the composite of magnetite nanoparticles and coordination fullerene-Pd(0) polymer as a model material for deposition on a magnetic electrode. Magnetite plays a dual role in this material, ensuring the nanostructured morphology of the composite and imparting magnetic activity to the composite, enabling the material to be deposited on the surface of the electrode in a magnetic field. The electrochemical behavior of the electrode modified with a pure coordination fullerene-Pd(0) polymer and the electrode modified with a composite of this polymer and magnetite are compared, highlighting the advantages of the second approach.

2. Results and Discussion

2.1. Structural Studies of the Fe_3O_4-$\gamma Fe_2O_3/(C_{60}Pd_3)_n$ Composite

The transmission electron microscopy (TEM) images of the composite composed of iron oxide magnetic nanoparticles and $(C_{60}Pd_3)_n$ polymeric particles obtained for different amounts of magnetite in the growth solution and separate components of the composite are presented in **Figure 1**. Magnetite forms spherical particles with diameters of ≈20 nm. A particle size distribution diagram presented as an insert in Figure 1a shows a relatively narrow range of magnetite diameter sizes. The $(C_{60}Pd_3)_n$ polymer is precipitated from the benzene solution containing the Pd(0) complex and fullerene C_{60} in the form of large cubic structures composed of small spherical particles.[76] These large cubic structures can be decomposed into a stable dispersion of spherical particles ≈70–100 nm in diameter (Figure 1b). In the composites (panels c–f of Figure 1), both magnetite and the $(C_{60}Pd_3)_n$ polymer preserve their morphology. Larger polymeric nanoparticles are deposited at the agglomerates of magnetite nanoparticles. However, the size of the $(C_{60}Pd_3)_n$ nanoparticles in the composite is lower in comparison to the size of particles formed in solution, which does not contain magnetite nanoparticles. It is very likely that polymerization takes place at the surface of these iron oxide magnetic nanoparticle agglomerates.

In **Figure 2**, the X-ray powder diffraction (XRD) patterns recorded for the $(C_{60}Pd_3)_n$ polymer and iron oxide magnetic nanoparticle and $(C_{60}Pd_3)_n$ polymeric particle composites formed in solutions containing different amounts of magnetite nanoparticles are presented. In the diffraction pattern of the $(C_{60}Pd_3)_n$ polymer, very broad and weak reflections are observed
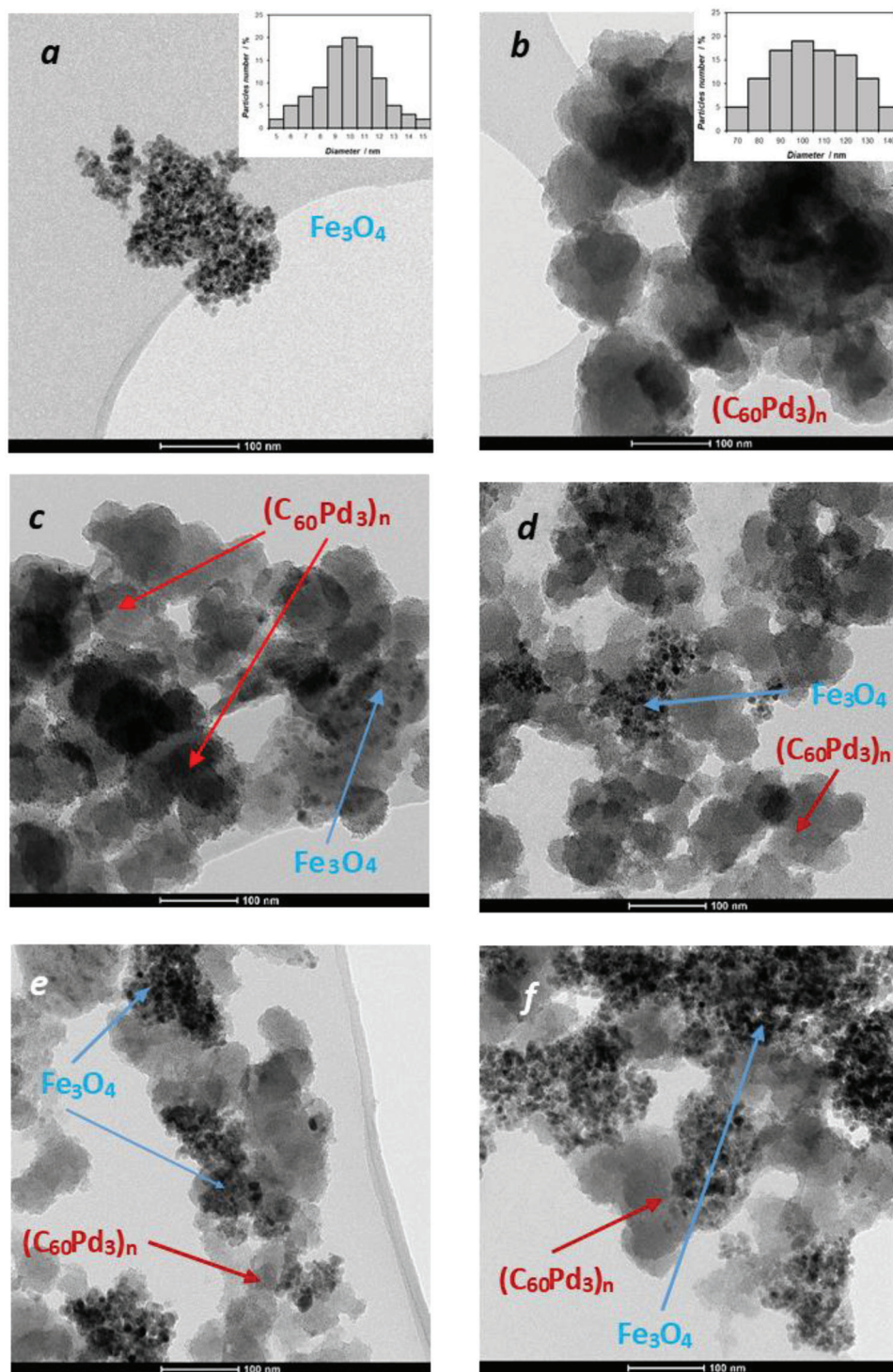
ADVANCED
SCIENCE NEWS
www.advancedsciencenews.com

[M]acro-molecular
Rapid Communications
www.mrc-journal.de

Figure 1. Transmission electron microscopy images of a) Fe_3O_4-γFe_2O_3 nanoparticles, b) chemically formed $(C_{60}Pd_3)_n$ polymer, and Fe_3O_4-$\gamma Fe_2O_3/(C_{60}Pd_3)_n$ composites formed in 20 mL of benzene solution containing 0.48×10^{-3} M C_{60}, 0.72×10^{-3} M $Pd_2(dba)_3 \cdot CHCl_3$, and c) 2 mg Fe_3O_4-γFe_2O_3, d) 5 mg Fe_3O_4-γFe_2O_3, e) 10 mg Fe_3O_4-γFe_2O_3, and f) 20 mg Fe_3O_4-γFe_2O_3. The insets show the size distributions of the a) magnetite nanoparticles and b) $(C_{60}Pd_3)_n$ polymer.

ADVANCED
SCIENCE NEWS
www.advancedsciencenews.com
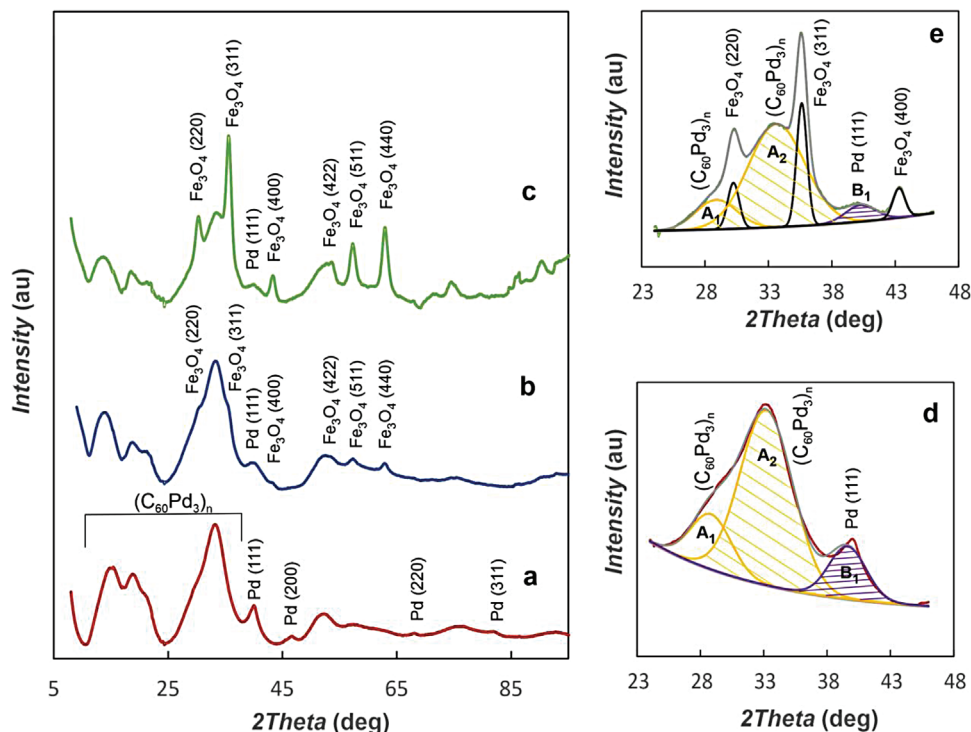
[M]acro-molecular
Rapid Communications
www.mrc-journal.de

Figure 2. XRD patterns of a) $(C_{60}Pd_3)_n$ polymer and Fe_3O_4-γFe_2O_3 /$(C_{60}Pd_3)_n$ composites formed in 20 mL of benzene solution containing 0.48×10^{-3} M C_{60}, 0.72×10^{-3} M $Pd_2(dba)_3 \cdot CHCl_3$ and b) 2 mg Fe_3O_4-γFe_2O_3, and c) 10 mg Fe_3O_4-γFe_2O_3. Deconvoluted diffractograms od d) $(C_{60}Pd_3)_n$ polymer and e) Fe_3O_4-$\gamma Fe_2)_3$/$(C_{60}Pd_3)_n$ composite formed in 20 mL of benzene solution containing 0.48×10^{-3} M C_{60}, 0.72×10^{-3} M $Pd_2(dba)_3 \cdot CHCl_3$ and 10 mg Fe_3O_4-γFe_2O_3.

at 15.4, 19.0, 20.8, and 33.3 2Theta. According to Talyzin et al.,[87] these peaks originate from the structure of $(C_{60}Pd_3)_n$, in which fullerene moieties are coordinated to the six palladium atoms in an octahedral fashion. They are not indexable due to their shape and broad width. Some weak peaks at 40.0, 46.6, 68.0, and 82.0 2Theta are also observed in the XRD patterns. They can be assigned to four reflection indices of (111), (200), (220), and (311), respectively, of the cubic crystal lattice structure of metallic Pd with the space group Fm3m (No.225) (PDF Card 461 043). The width and intensity of these peaks indicate the formation of a small amount of Pd nanoparticles in the samples. In patterns b and c recorded for composites with iron oxide nanoparticles, reflections characteristic of the polymer $(C_{60}Pd_3)_n$ are observed at 13.8, 18.6, 21.2, and 33.3 2Theta. Additionally, there are peaks assigned to reflection indices of (220), (311), (400), (422), (511), and (440) of iron oxide nanoparticles (magnetite or maghemite) crystallizing in the cubic spinel structure with a similar lattice parameters (magnetite $q = 0.8396$ nm and maghemite $a = 0.83 474$ nm).[88] Iron oxide magnetic nanoparticles, magnetite and maghemite, cannot be distinguished easily using standard X-ray diffraction techniques since the crystal structure of both of these oxides is very similar.[89] Therefore, magnetic iron oxide nanoparticles will be denoted as Fe_3O_4-γFe_2O_3.

The intensity of the peaks recorded for iron oxide nanoparticles increases as the magnetite content in the composite increases. In the presence of iron oxide nanoparticles, the intensity of the reflections for metallic Pd decreases, and only the characteristic peak at 40.0 2Theta is slightly visible on the patterns.

The ratio of the amounts of composite components can be determined by comparing the areas under the diffraction peaks. For this purpose, the signals were extracted by deconvolution in the range from 25 to 45 2Theta. Exemplary results of deconvolution of diffractograms are shown in Figure 2 for a fullerene coordination polymer (panel d) and a composite of magnetite and $(C_{60}Pd_3)_n$ polymer (panel e). The ratio of the areas of Pd(111) peak and diffraction peak corresponding to the $(C_{60}Pd_3)_n$ polymer decreases with the increase of the amount of magnetite nanoparticles in solution during polymer formation (**Table 1**). The decrease in metallic Pd content indicates that the stoichiometry of the $(C_{60}Pd_3)_n$ polymer formed in a solution containing iron oxide nanoparticles is much closer to the theoretical value than that of the polymer synthesized without Fe_3O_4-γFe_2O_3. The sizes of metal nanoparticles determined on the basis of the Scherrer method assuming their spherical shape remains practically constant.

In order to check the quality of the iron oxide nanoparticles and composition of formed composite, the Mössbauer spectroscopy was used. The measured spectra without and with external magnetic field $B = 1.3T$ parallel to gamma beam direction are presented in **Figure 3**. For the iron oxide nanoparticles (panel a), the spectra measured without external magnetic field show the broad lines as a result of superparamagnetic fluctuation of the Fe magnetic moments. Such behavior is typical for nanoparticles at room temperature. The spectrum measured in external magnetic field is sharp and the individual three sextets are visible which comes from Fe located in [A], [B] sites of spinel structure

**ADVANCED
SCIENCE NEWS**

www.advancedsciencenews.com

{[M]} macro-
molecular
Rapid Communications

www.mrc-journal.de

Table 1. Influence of the magnetite on the polymeric phase composition in the Fe_3O_4-$\gamma Fe_2O_3/(C_{60}Pd_3)_n$ composite.

Polymerization conditions[a]	Area under A_2 peak [au] $(C_{60}Pd_3)_n$	Area under B_1 peak [au] Pd(111)	B_1/A_2	Pd particle diameter [nm][b]
0.48×10^{-3} M C_{60}, 0.72×10^{-3} M $Pd_2(dba)_3$·$CHCl_3$	8.32	1.76	0.21	4.2
0.48×10^{-3} M C_{60}, 0.72×10^{-3} M $Pd_2(dba)_3$·$CHCl_3$ + 2 mg Fe_3O_4-γFe_2O_3	9.96	1.27	0.12	3.2
0.48×10^{-3} M C_{60}, 0.72×10^{-3} M $Pd_2(dba)_3$·$CHCl_3$ + 10 mg Fe_3O_4-γFe_2O_3	9.45	0.81	0.09	4.4

[a] 20 mL of benzene. [b] Calculated using Scherrer equation $D = K\lambda/\beta\cos\theta$, where D is Pd particle diameter, K is Scherrer constant for spherical particles, λ is the X-ray wavelength, and β is the line broadening at the full width half maxima

and on the surface (broad sextet). It is a result of suppressing of the Fe magnetic moments fluctuations by applied external field. Such shape of spectrum are typical for maghemite nanoparticles $(Fe^{3+})_A[Fe^{3+}_{5/3} \blacksquare_{1/3}]_BO_4$, where $\blacksquare$ means cation vacancies.[90,91] Therefore, the Mössbauer spectroscopy studies indicate partial oxidation of magnetite to maghemite during the iron oxide nanoparticles preparation. The intensities 5th and 2nd lines in measured spectrum disappear as a result of ordering of Fe moment parallel to external field direction. It means that obtained nanoparticles are very soft from magnetic point of view. Similar magnetic behavior was observed for iron oxide particles incorporated into composite with $(C_{60}Pd_3)_n$ polymer (panel b of Figure 3). The small changes in the shapes of the spectra compared to previous ones are caused by the smaller dipole–dipole interaction between maghemite nanoparticles incorporated into composite. Mössbauer spectrum recorded for this material also shows the presence of magnetic maghemite in the composite.

The composition of the Fe_3O_4-$\gamma Fe_2O_3/(C_{60}Pd_3)_n$ nanocomposite was also confirmed by FT-IR spectroscopy (**Figure 4**). The two intense peaks observed at 585 and 635 cm^{-1} in the IR spectrum of Fe_3O_4 (Figure 4a) are attributed to the stretching vibration mode associated to the metal-oxygen Fe–O bonds in the crystalline lattice of magnetite.[92] The band at 1630 cm^{-1} and the

broad band centered at $\approx$3430 cm^{-1} are related to the presence of hydroxyl groups due to the magnetite surface hydrolyzation and attributed to OH-bending and OH-stretching, respectively.[92] In the spectrum of pure $(C_{60}Pd_3)_n$ polymer (Figure 4b), the characteristic bands at 517 and 669 cm^{-1} are assigned to the fullerene cage deformation vibrations.[93] The vibration at 1367 cm^{-1} can be attributed to the vibrations of the coordinated C=C bond. The low intensity of this signal indicates that palladium is coordinated symmetrically at the center of this bond. The signal at 1450 cm^{-1} is assigned to the stretching of C=C bonds which are not coordinated to palladium atoms. The spectrum of Fe_3O_4-$\gamma Fe_2O_3/(C_{60}Pd_3)_n$ nanocomposite (Figure 4c) clearly shows characteristic peaks of both Fe_3O_4-γFe_2O_3 nanoparticles and pure coordination fullerene polymer. A small shifts of some absorption bands towards higher wave numbers in the spectrum of the composite in relation to the spectra obtained for its components indicates weak interactions between the magnetite and the $(C_{60}Pd_3)_n$ layer.

The quantitative composition of Fe_3O_4-$\gamma Fe_2O_3/(C_{60}Pd_3)_n$ composites formed in dispersions containing different amounts of magnetite nanoparticles was investigated using the thermogravimetric analysis (TGA) technique. The curves of the relative mass versus temperature for the obtained composites are shown in **Figure 5**. For comparison, the thermogravimetric curves recorded for the magnetite nanoparticles and pure $(C_{60}Pd_3)_n$ polymer are also presented. Fe_3O_4-γFe_2O_3 is stable from 20 °C to 1050 °C. The $(C_{60}Pd_3)_n$ polymeric material is decomposed at
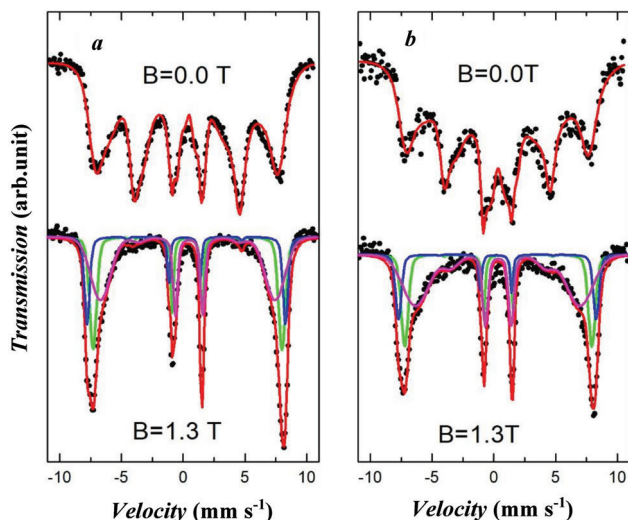
Figure 3. Mössbauer spectra of a) iron oxide nanoparticles and b) Fe_3O_4-$\gamma Fe_2O_3/(C_{60}Pd_3)_n$ composites formed in 20 mL of benzene solution containing 0.48×10^{-3} M C_{60}, 0.72×10^{-3} M $Pd_2(dba)_3$·$CHCl_3$, and 10 mg Fe_3O_4-γFe_2O_3 measured without and with external magnetic field parallel to gamma beam direction.

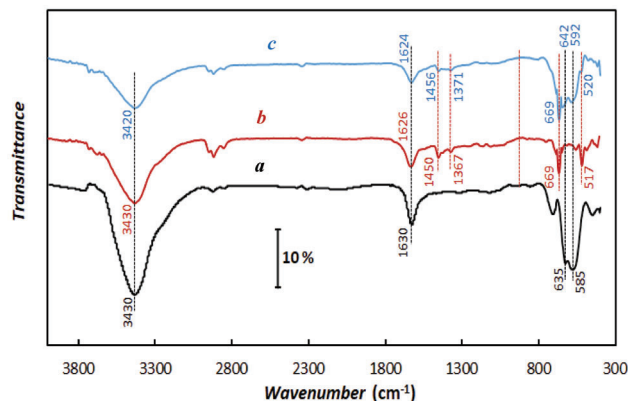**Figure 4.** FT-IR spectra of a) Fe_3O_4-γFe_2O_3 nanoparticles, b) $(C_{60}Pd_3)_n$ chemically formed in 20 mL of benzene solution containing 0.48×10^{-3} M C_{60}, 0.72×10^{-3} M $Pd_2(dba)_3$·$CHCl_3$, and c) Fe_3O_4-$\gamma Fe_2O_3/(C_{60}Pd_3)_n$ nanocomposite formed in 20 mL of benzene solution containing 0,48 x 10^{-3} M C_{60}, 0.72×10^{-3} M $Pd_2(dba)_3$·$CHCl_3$, and 10 mg Fe_3O_4-γFe_2O_3.

ADVANCED
SCIENCE NEWS
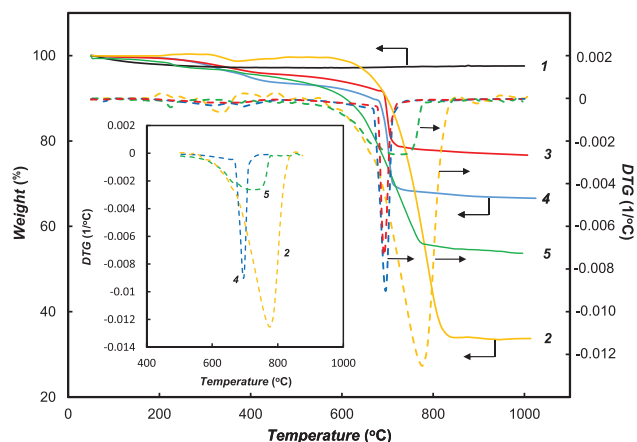www.advancedsciencenews.com

[M] acro-
molecular
Rapid Communications
www.mrc-journal.de

Figure 5. Thermogravimetric analysis (TGA) (solid lines) and DTG (dashed lines) curves of (1) Fe_3O_4-γFe_2O_3 nanoparticles, (2) pure $(C_{60}Pd_3)_n$ polymer, and (3–5) Fe_3O_4-$\gamma Fe_2O_3/(C_{60}Pd_3)_n$ nanocomposites recorded in an argon atmosphere. Composites were formed in 20 mL of benzene containing 0.48×10^{-3} M C_{60}, 0.72×10^{-3} M $Pd_2(dba)_3 \cdot CHCl_3$ and (3) 20 mg Fe_3O_4-γFe_2O_3, (4) 10 mg Fe_3O_4-γFe_2O_3, (5) 5 mg Fe_3O_4-γFe_2O_3 for 10 h. The inset shows the DTG responses of the $(C_{60}Pd_3)_n$ polymer and Fe_3O_4-$\gamma Fe_2O_3/(C_{60}Pd_3)_n$ nanocomposites in the temperature range of $(C_{60}Pd_3)_n$ decomposition.

temperatures higher than approximately 600 °C. The ratio of palladium to C_{60} calculated from the mass changes during polymeric material decomposition is close to approximately 3.5:1. This value indicates that the polymeric material contains particles of metallic palladium in addition to the pure polymer phase. The Fe_3O_4-$\gamma Fe_2O_3/(C_{60}Pd_3)_n$ composites also exhibit a single weight loss step corresponding to the $(C_{60}Pd_3)_n$ polymeric material decomposition. These mass changes allow us to estimate the mass percentage of the polymeric material in the mass of the formed composites. Appropriate values are given in **Table 2** for composites formed in suspensions containing different amounts of magnetite nanoparticles. The composition of the composite is also obtained from the mass of synthesized Fe_3O_4-$\gamma Fe_2O_3/(C_{60}Pd_3)_n$ composites. After quantitative separation of the composite from the postreaction solution, the precipitate is weighed, and the percentage content of its components is determined. The results obtained for various conditions of composite formation are summarized in Table 2. A good agreement between the results of composite composition determination based on TGA and composite mass is observed. The results of the influence of polymerization time on the amount of polymeric phase formation indicate that for times longer than approximately 10 h, the polymerization process is completed, and the mass of polymer in the composite reaches a constant value.

The results of TGA measurements presented in Figure 5 are quite intriguing. The inset in Figure 5 shows the DTG responses of the $(C_{60}Pd_3)_n$ polymer and Fe_3O_4-$\gamma Fe_2O_3/(C_{60}Pd_3)_n$ nanocomposites containing two different amounts of magnetite in the temperature range of that of $(C_{60}Pd_3)_n$ decomposition. The pure $(C_{60}Pd_3)_n$ polymer decomposes in a relatively broad temperature range of 250 °C. In contrast, the temperature range of the polymer incorporated into the composite containing a larger amount of magnetite decomposition is very narrow. The $(C_{60}Pd_3)_n$ is decomposed within the temperature window of 40 °C. Such behavior indicates that $(C_{60}Pd_3)_n$ polymeric phase that is deposited on the surface of magnetite nanoparticles is structurally much more homogeneous than that in the polymeric phase formed in the absence of magnetite. In the case of the composite containing small amounts of magnetite nanoparticles, the broad DTG peak is a component of two signals corresponding to different polymer phases.

Table 2. Composition of Fe_3O_4-$\gamma Fe_2O_3/(C_{60}Pd_3)_n$ formed under different experimental conditions obtained from the thermogravimetric analysis (TGA) measurements and mass of the formed composite

Polymerization conditions[a]	Polymerization time [h]	Percentage content of $(C_{60}Pd_3)_n$ in the composite [% w/w]
0.48×10^{-3} M C_{60}, 0.72×10^{-3} M $Pd_2(dba)_3 \cdot CHCl_3$ + 2 mg Fe_3O_4-γFe_2O_3	10	77[b] 80[c]
0.48×10^{-3} M C_{60}, 0.72×10^{-3} M $Pd_2(dba)_3 \cdot CHCl_3$ + 5 mg Fe_3O_4-γFe_2O_3	10	58[b] 59[c]
0.48×10^{-3} M C_{60}, 0.72×10^{-3} M $Pd_2(dba)_3 \cdot CHCl_3$ + 10 mg Fe_3O_4-γFe_2O_3	10	35[b] 39[c]
0.48×10^{-3} M C_{60}, 0.72×10^{-3} M $Pd_2(dba)_3 \cdot CHCl_3$ + 20 mg Fe_3O_4-γFe_2O_3	10	12[b] 14[c]
0.48×10^{-3} M C_{60}, 0.72×10^{-3} M $Pd_2(dba)_3 \cdot CHCl_3$ + 10 mg Fe_3O_4-γFe_2O_3	2	11[c]
0.48×10^{-3} M C_{60}, 0.72×10^{-3} M $Pd_2(dba)_3 \cdot CHCl_3$ + 10 mg Fe_3O_4-γFe_2O_3	4	22[c]
0.48×10^{-3} M C_{60}, 0.72×10^{-3} M $Pd_2(dba)_3 \cdot CHCl_3$ + 10 mg Fe_3O_4-γFe_2O_3	10	37[c]
0.48×10^{-3} M C_{60}, 0.72×10^{-3} M $Pd_2(dba)_3 \cdot CHCl_3$ + 10 mg Fe_3O_4-γFe_2O_3	16	42[c]
0.48×10^{-3} M C_{60}, 0.72×10^{-3} M $Pd_2(dba)_3 \cdot CHCl_3$ + 10 mg Fe_3O_4-γFe_2O_3	19	39[c]

[a] 20 mL of benzene. [b] From the TGA measurements. [c] Based on the mass of composite.

**ADVANCED
SCIENCE NEWS**

www.advancedsciencenews.com

[M] acro-
olecular
Rapid Communications

www.mrc-journal.de
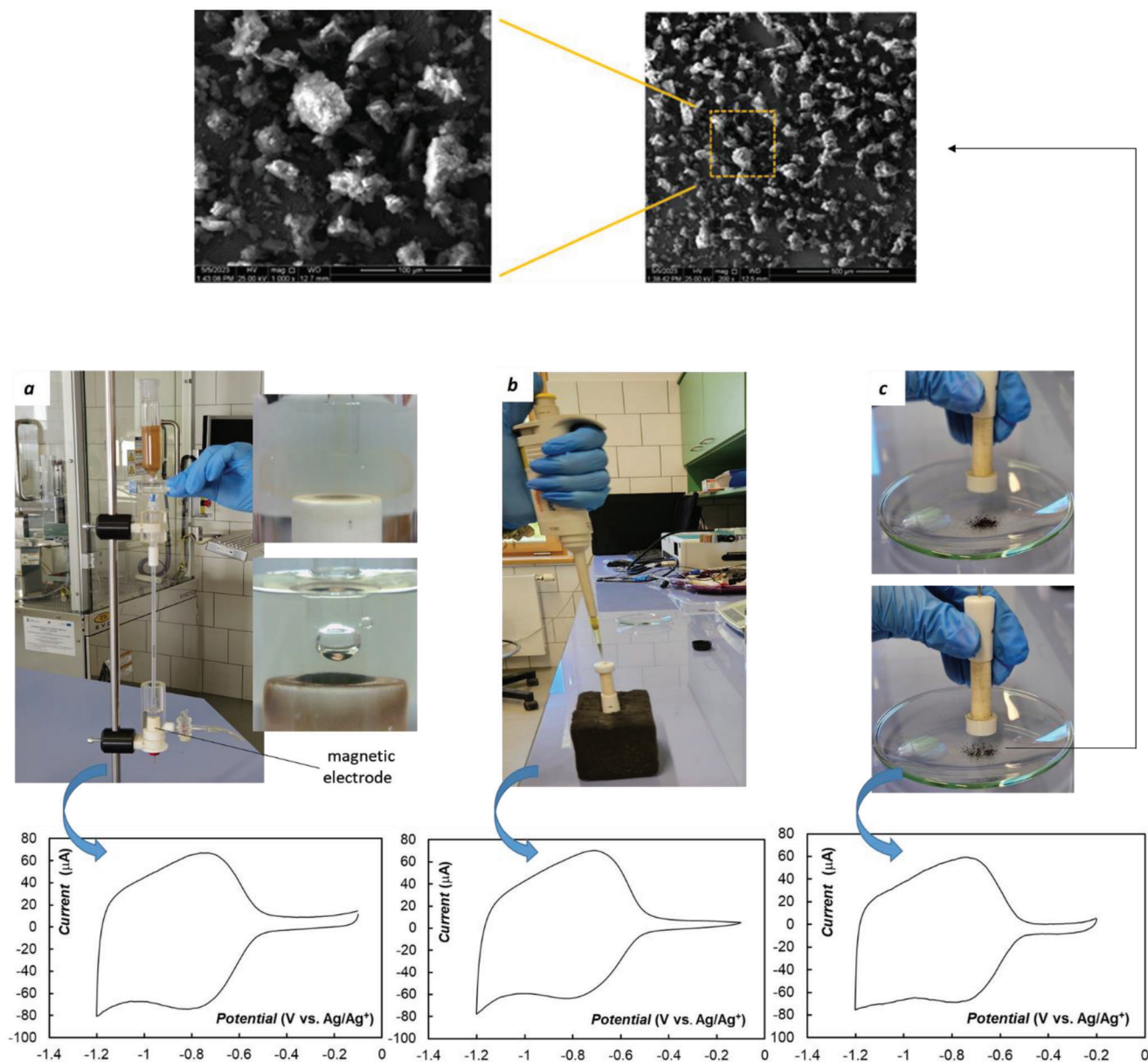
Figure 6. Illustration of different methods of Fe_3O_4-$\gamma Fe_2O_3/(C_{60}Pd_3)_n$ composite deposition on the surface of the magnetic electrode and corresponding voltammetric responses in acetonitrile containing 0.1 M (n-$C_4H_9)_4NClO_4$ at 0.1 V s^{-1}. a) Deposition in the liquid phase, b) drop coating method, and c) solid-phase solvent-free deposition. SEM images of the magnetite electrode surface coated with Fe_3O_4-$\gamma Fe_2O_3/(C_{60}Pd_3)_n$ composite at two different magnifications.

2.2. Electrochemical Investigation of the Fe_3O_4-$\gamma Fe_2O_3/(C_{60}Pd_3)_n$ Composite

2.2.1. Voltammetry

The magnetic material can be deposited at the electrode surface in various ways. In **Figure 6**, three methods of Fe_3O_4-$\gamma Fe_2O_3/(C_{60}Pd_3)_n$ composite deposition are shown. The surface of the gold electrode can be modified both in solution (panel a) and out of solution (panels b and c) with a magnetic material. It is also possible to deposit the material both from the solution (panels a and b) and from the solid phase (panel c). The method of

electroactive material deposition on the surface of the magnetic electrode does not affect its electrochemical properties, as shown in the voltammograms presented in Figure 6.

The voltammetric responses of the Fe_3O_4-$\gamma Fe_2O_3/(C_{60}Pd_3)_n$ composite and $(C_{60}Pd_3)_n$ polymeric material deposited at the surface of the magnetic electrode are compared in **Figure 7**. The voltammograms presented in this figure were recorded for thin films containing the same amount of the $(C_{60}Pd_3)_n$ polymer. The composite was magnetically bonded to the electrode surface. The pure $(C_{60}Pd_3)_n$ polymer was weakly mechanically connected with the gold electrode surface. Both materials are electrochemically active at negative potentials due to fullerene moiety reduction. In
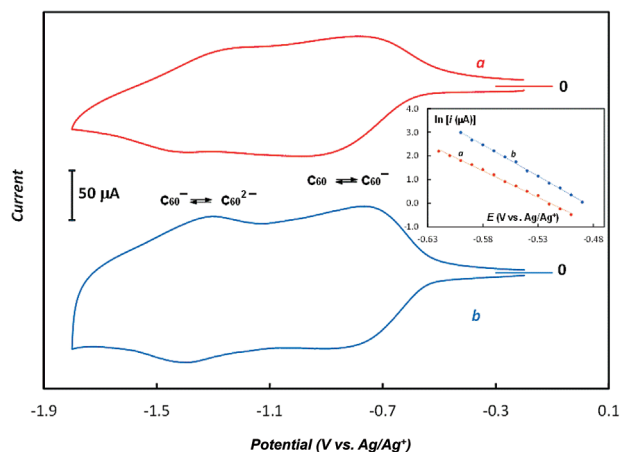
ADVANCED
SCIENCE NEWS

www.advancedsciencenews.com

[M] acro-
molecular
Rapid Communications

www.mrc-journal.de

Figure 7. Cyclic voltammograms of magnetic electrode coated with a) $(C_{60}Pd_3)_n$ polymer and b) Fe_3O_4-$\gamma Fe_2O_3/(C_{60}Pd_3)_n$ composite at 0.1 V s^{-1} in acetonitrile containing 0.1 M $(n\text{-}C_4H_9)_4NClO_4$. Composites were formed in 20 mL of benzene containing 0.48×10^{-3} M C_{60}, 0.72×10^{-3} M $Pd_2(dba)_3 \cdot CHCl_3$, and 10 mg of Fe_3O_4-γFe_2O_3 for 10 h. Inset shows the ln i–E relationship for the first 15% of the peak corresponding to the first electron exchange for the electrode covered with a) $(C_{60}Pd_3)_n$ polymer and b) Fe_3O_4-$\gamma Fe_2O_3/(C_{60}Pd_3)_n$ composite.

the studied potential range, two reduction steps corresponding to the formation of C_{60}^- and C_{60}^{2-} centers in the polymeric backbone are observed. The voltammetric signals corresponding to the first two fullerene moiety-involved charge exchange processes are much better developed in the case of the composite. The redox processes are also much more reversible in the case of the magnetic Fe_3O_4-$\gamma Fe_2O_3/(C_{60}Pd_3)_n$ composite in comparison to $(C_{60}Pd_3)_n$. The rate of the polymeric phase reduction can be expressed by the slope of the relation between the logarithm of the reduction current and the potential in the potential range of the oxidation peak formation (approximately the first 15% of the high peak oxidation). Such relations are shown in the inset in Figure 7. The value of the ln i_{red} – E slope is much higher in the case of the Fe_3O_4-$\gamma Fe_2O_3/(C_{60}Pd_3)_n$ nanocomposite in comparison to the one obtained for the electrode modified with pure chemically formed $(C_{60}Pd_3)_n$ polymer.

In **Figure 8**, the investigation of the sweep rate effect on the voltammetric behavior of the $(C_{60}Pd_3)_n$ polymer and Fe_3O_4-$\gamma Fe_2O_3/(C_{60}Pd_3)_n$ composite is presented. The polymeric phase reduction current linearly depends on the sweep rate (v), indicating that the material concentrated at the electrode surface is involved in the electrode processes. The slope of the i_p – v relation is higher in the case of the Fe_3O_4-$\gamma Fe_2O_3/(C_{60}Pd_3)_n$ composite indicating a higher degree of the electrochemically active material reduction in the case of composite in comparison to pure polymeric material. Additionally, a much lower separation between peak reduction and oxidation potential is observed for the composite. In lower right panel of Figure 8, the dependence of peak potential separation on the sweep rate is shown for both studied materials. Such relations are shown for the first fullerene reduction process. In the case of the second reduction step, the voltammetric peaks are poorly developed, particularly for the $(C_{60}Pd_3)_n$ polymer, preventing such an analysis. The pure $(C_{60}Pd_3)_n$ polymer exhibits a higher separation between potentials of anodic and ca-

thodic peak currents. Additionally, the difference in cathodic and anodic peak current potentials increases much faster with the increase in the sweep rate for the polymer compared to the composite. Such behavior indicates that the fullerene polymer-involved charge transfer process is much faster when the polymeric material forms a nanoscale composite with the magnetite nanoparticle. The enhancement of the electrochemical performance of the composite in comparison to the pure polymeric material is related both to the stronger interaction of the composite with the magnetic electrode and the nanostructured morphology of the Fe_3O_4-$\gamma Fe_2O_3/(C_{60}Pd_3)_n$ material.

In **Figure 9**, voltammetric responses of the Fe_3O_4-$\gamma Fe_2O_3/(C_{60}Pd_3)_n$ composite formed in solutions containing different amounts of Fe_3O_4-γFe_2O_3 nanoparticles are presented. The voltammograms were recorded in the potential range of the first fullerene moiety reduction step. The voltammograms were recorded with the same mass of composite material. The composite was deposited at the magnetic electrode surface from the solid phase. Even composites with a low content of the magnetic component are effectively and quantitatively deposited on the surface of the magnetic electrode. The current corresponding to the first fullerene reduction step increases with an increase in the amount of magnetite component in the composite. This is a rather unexpected behavior because higher currents are observed for materials containing a smaller amount of polymer phase. This behavior is the result of a greater degree of active surface
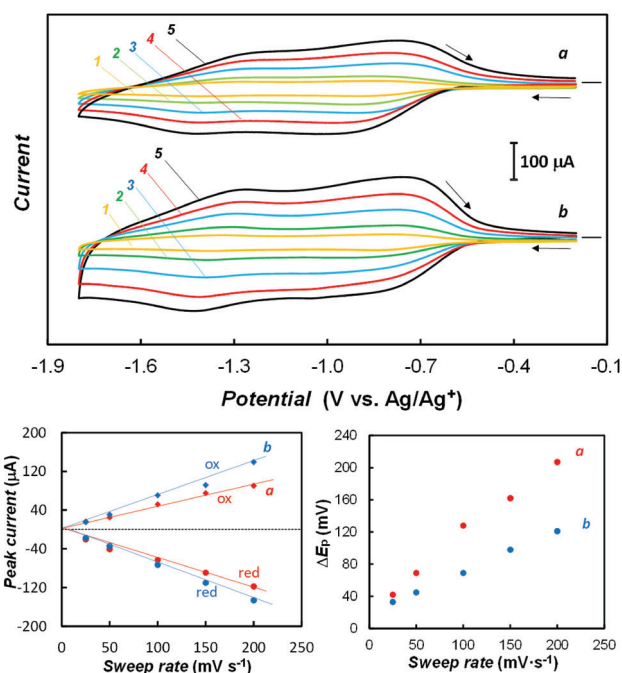

Figure 8. Cyclic voltammograms (upper panel) of magnetic electrode coated with a) $(C_{60}Pd_3)_n$ polymer and b) Fe_3O_4-$\gamma Fe_2O_3/(C_{60}Pd_3)_n$ composite at (1) 25, (2) 50, (3) 100, (4) 150, and (5) 200 mV s^{-1} in acetonitrile containing 0.1 mL dm^{-3} $(n\text{-}C_4H_9)_4NClO_4$. Dependence of the peak current of the first C_{60} reduction step on the sweep rate (bottom left) and peak separation potentials on the sweep rate (bottom right) for the a) $(C_{60}Pd_3)_n$ polymer and b) Fe_3O_4-$\gamma Fe_2O_3/(C_{60}Pd_3)_n$ composite. Composites were formed in 20 mL of benzene containing 0.48×10^{-3} M C_{60}, 0.72×10^{-3} M $Pd_2(dba)_3 \cdot CHCl_3$ and 10 mg of Fe_3O_4-γFe_2O_3 for 10 h.

**ADVANCED
SCIENCE NEWS**

www.advancedsciencenews.com

{M} acro-
olecular
Rapid Communications

www.mrc-journal.de
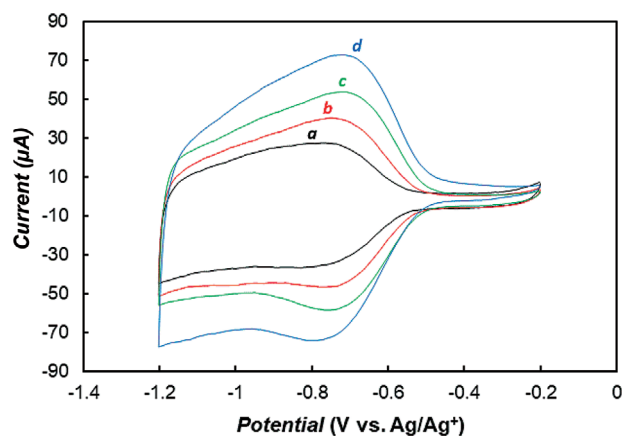
Figure 9. Cyclic voltammograms of magnetic electrode coated with Fe_3O_4-γFe_2O_3/$(C_{60}Pd_3)_n$ composite formed in 20 mL of benzene containing 0.48×10^{-3} M C_{60}, 0.72×10^{-3} M $Pd_2(dba)_3 \cdot CHCl_3$, and a) 2 mg Fe_3O_4-γFe_2O_3, b) 5 mg Fe_3O_4-γFe_2O_3, c) 10 mg Fe_3O_4-γFe_2O_3, and d) 20 mg of Fe_3O_4-γFe_2O_3 for 10 h at 0.1 V s^{-1} in acetonitrile containing 0.1 M $(n\text{-}C_4H_9)_4NClO_4$.

area development of the composite containing larger amounts of magnetite nanoparticles. An increase in the difference between the reduction and oxidation peak potential of the polymer is also observed along with the increase in the magnetite content in the composite resulting from the nonconductive nature of the magnetite nanoparticles.

The current density of the composite material immobilized at the electrode surface linearly depends on the amount of material deposited at the electrode surface (**Figure 10**). Such behavior indicates that in 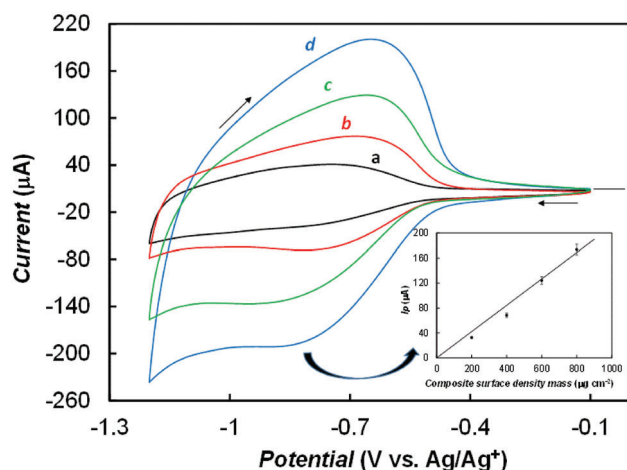the studied surface density mass range, the whole material undergoes the process of electro-reduction. The peak potentials of cathodic and anodic processes are shifted toward more negative and less negative potentials, respectively. Such an effect is probably related to the increasing resistance of ion transfer processes with increasing composite layer thickness. Despite this potential shift, the voltammetric curves retain the typical shape for electrode processes involving conductive polymers.

The method of immobilizing the electroactive phase on the surface of the electrode affects not only the mechanical durability of the deposited layer but also the stability of its electrochemical properties. The $(C_{60}Pd_3)_n$ polymer is doped with the cations of the supporting electrolyte during the reduction process. The incorporation of large tetra(alkyl)ammonium cations into the polymer structure causes morphological changes leading to polymer decomposition. In addition, the negative charge located on the fullerene units reduces the stability of the polymer chain. The stability of the film formed from chemically produced $(C_{60}Pd_3)_n$ polymer is very limited. It slowly decomposes during charging in the potential range of the first two fullerene moiety reduction steps. Upon multicyclic potential sweep, a gradual decrease in both reduction and oxidation currents in this potential range is observed (voltammogram a in **Figure 11**). Therefore, the currents of polymer-involved redox charge transfer processes reach a stable but very low value after the 15th voltammetric cycle. The magnetic Fe_3O_4-γFe_2O_3/$(C_{60}Pd_3)_n$ composite exhibits more stable voltammetric behavior (upper voltammogram of panel b in Figure 11). In the potential range of the first two electron transfer steps, this material exhibits stable behavior despite larger charges related to these electrode processes. Polymer decomposition is observed during polarization to the potential range of the third fullerene-involved reduction step (lower voltammogram of panel c in Figure 11).

Figure 10. Cyclic voltammograms of the magnetic electrode coated with the Fe_3O_4-γFe_2O_3/$(C_{60}Pd_3)_n$ composite formed in 20 mL of benzene containing 0.48×10^{-3} M C_{60}, 0.72×10^{-3} M $Pd_2(dba)_3 \cdot CHCl_3$ and 10 mg Fe_3O_4-γFe_2O_3 at 0.1 V s^{-1} in acetonitrile containing 0.1 M $(n\text{-}C_4H_9)_4NClO_4$. Composite surface mass densities of a) 204, b) 408, c) 611, and d) 815 $\mu g\ cm^{-2}$. The inset shows the relation between the cathodic peak current and the mass of the composite deposited at the electrode surface.

Figure 11. Multicyclic voltammograms of magnetic electrode coated with a) $(C_{60}Pd_3)_n$ polymer and b) Fe_3O_4-γFe_2O_3/$(C_{60}Pd_3)_n$ composite formed in 20 mL of benzene containing 0.48×10^{-3} M C_{60}, 0.72×10^{-3} M $Pd_2(dba)_3 \cdot CHCl_3$ and 10 mg Fe_3O_4-γFe_2O_3, in acetonitrile containing 0.1 M $(n\text{-}C_4H_9)_4NClO_4$ for two potential ranges at 0.1 V s^{-1}.

2.2.2. Impedance

The electrochemical properties of the Fe_3O_4-$\gamma Fe_2O_3/(C_{60}Pd_3)_n$ nanocomposite were also studied by electrochemical impedance spectroscopy. **Figure 12** presents the imaginary part of impedance, Z'', as a function of the real part of impedance, Z', for the $(C_{60}Pd_3)_n$ polymeric material (panel a) and Fe_3O_4-$\gamma Fe_2O_3/(C_{60}Pd_3)_n$ composite (panel b) deposited at the magnetic electrode surface. The Z''–Z' responses were obtained for different reduction potentials. The potential profiles applied in the faradaic impedance studies are shown in an inset in panel a of Figure 12. The measurement of the impedance for each measured frequency of potential changes at a constant reduction potential of the polymer E_R was preceded by keeping the electrode at the potential E_i, enabling the polymer to return to its nonreduced form. The composite/electrolyte interphase can be represented by the equivalent circuit shown in panel b of Figure 12 (inset). R_i is a solution resistance, R_{ct} represents the charge transfer resistance related to the $(C_{60}Pd_3)_n$ polymer reduction, and C_{dl} is the double-layer capacitance of the external interphase between the composite and electrolyte. The C_L capacitance represents the capacitance of the internal interphase between the electrode surface and solution inside the micropores and Z_W is the Warburg impedance related to counterion transport accompanying the polymer reduction process expressed by the following equation:

$$Z_W = \frac{1}{Y_0 \sqrt{j\omega}} \tag{1}$$

where $\omega = 2\pi f$ and Y_0 is the diffusion admittance expressed as follows:

$$\frac{1}{Y_0} = \sqrt{\frac{3 R_L}{C_L}} \tag{2}$$

In this equation R_L represents the resistance related to the ion transport process within the pores of electroactive material.

This equivalent circuit can be used to describe the electrode processes taking place in both the composite material and polymer. The solid lines presented in Figure 12 represent impedance changes simulated for the equivalent circuit. The correlation between the experimentally and theoretically obtained Z''–Z' relationships shows that the proposed theoretical model provides an accurate description of our material. The values of the equivalent circuit components used for the experimental data simulation for the pure polymer and Fe_3O_4-$\gamma Fe_2O_3/(C_{60}Pd_3)_n$ composite are displayed in **Table 3**.

A significant difference between the impedance responses of the electrode coated with the $(C_{60}Pd_3)_n$ polymer (panel a of Figure 12) and the magnetic electrode modified with the Fe_3O_4-$\gamma Fe_2O_3/(C_{60}Pd_3)_n$ composite (panel b of Figure 12) is observed. The impedance responses of the electrode coated with the composite are dominated by the capacitance properties of the material. The imaginary part of impedance increases rapidly with a decrease in frequency (panel a of Figure 12). In the high-frequency range, the semicircle related to the charge transfer resistance is very poorly developed due to the low charge transfer resistance and high contribution of the capacitance component. As a conse-

quence, the determination error of the R_{ct} value is relatively high (Table 3). As expected, the R_{ct} values decrease with the shift of potential toward more negative values.

In the case of pure polymeric material, three frequency ranges corresponding to different electrode processes can be selected. In the high-frequency range (inset in panel a of Figure 12), a poorly developed semicircle corresponding to the charge transfer resistance is observed. The charge transfer resistance values obtained for the Fe_3O_4-$\gamma Fe_2O_3/(C_{60}Pd_3)_n$ composite are lower than those obtained for the pure $(C_{60}Pd_3)_n$ polymer, which is not magnetically bound to the electrode surface. This charge transfer frequency range is followed by the frequency range of counterion diffusion which depends on the diffusion coefficient of the ions incorporated into the polymeric phase. The slope of the Z'–Z'' responses is close to 45° (dashed straight line in the insert graph). The Warburg impedance for this process is approximately an order of magnitude lower for the pure polymer than the composite. This indicates much easier transport of the base electrolyte ions into the electroactive phase in the composite material. Finally, the imaginary part of the frequency starts to increase due to the dominant share of capacitive processes. Large differences in the Warburg impedance are also observed. It should be noted that the capacitance properties of the composite are enhanced in comparison to the $(C_{60}Pd_3)_n$ polymer-modified electrode.

3. Conclusions

The magnetic composite material Fe_3O_4-$\gamma Fe_2O_3/(C_{60}Pd_3)_n$ was used as a model system to investigate its deposition on a magnetic electrode and its electrochemical properties. The nanoparticle magnetite ensures both the magnetic activity of the composite and its nanostructured morphology. Both of these factors are responsible for the enhancement of the electrochemical activity of the polymer phase forming the composite in comparison to the pure polymer material deposited on the same magnetic electrode. In the magnetic field of the electrode, the composite undergoes permanent and strong bonding with the surface of the electrode. This allows easy manipulation of the electrode, transferring it from one solution to another without losing the electroactive material from the electrode surface. This is of particular importance when such a magnetic electrode is used in the formation of electrochemical chemo(bio)sensors.

Significant changes in the electrochemical properties of the Fe_3O_4-$\gamma Fe_2O_3/(C_{60}Pd_3)_n$ composite immobilized on the surface of the magnetic electrode in comparison to the redox properties of the pure $(C_{60}Pd_3)_n$ polymer are observed. Under cyclic voltammetry conditions, the composite exhibits much more reversible redox properties in the potential range of the fullerene moiety reduction than that of the pure polymer. In the case of the composite, the current related to polymer phase reduction is also enhanced. This effect is related to the greater efficiency of doping the composite material with counterions from the electrolyte solution in addition to the reduction of the thin polymer layer deposited on the magnetite aggregates. The potential range of stable electrochemical behavior is also wider for the composite than for the pure polymer.
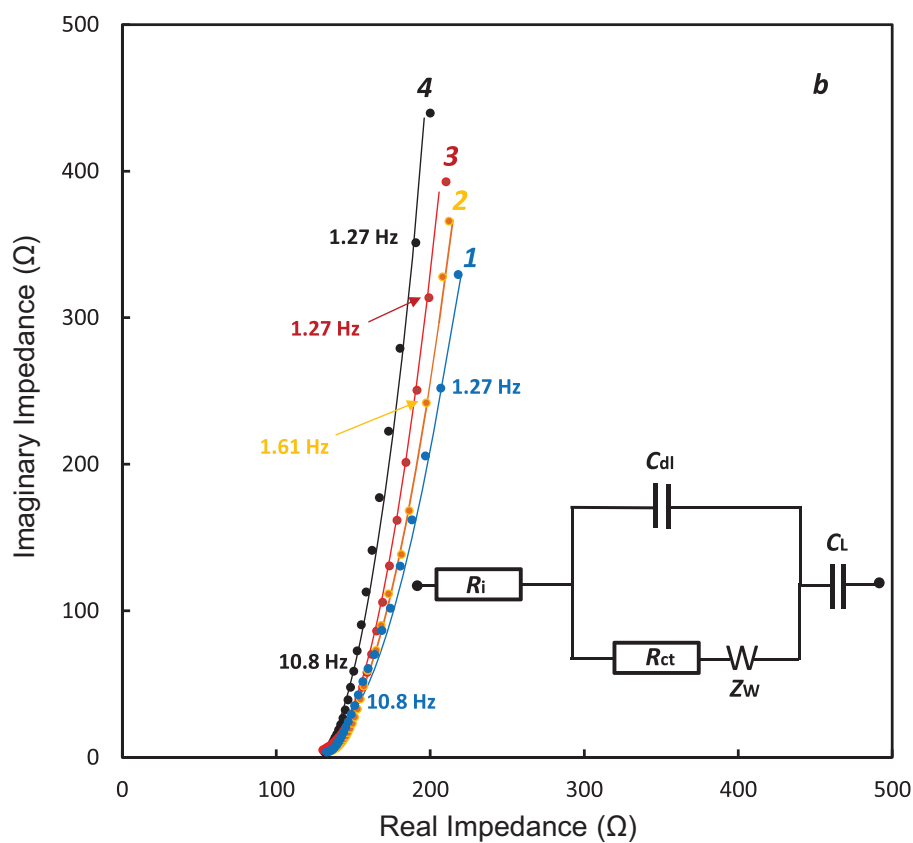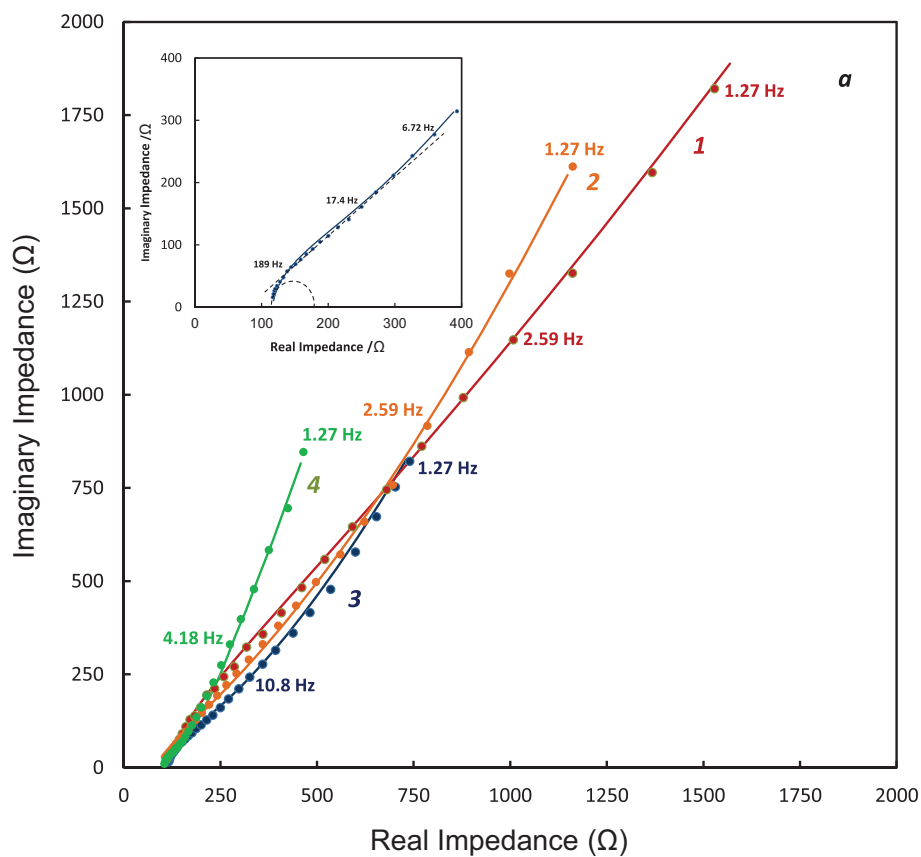
**ADVANCED
SCIENCE NEWS**

www.advancedsciencenews.com

[M] acro-
molecular
Rapid Communications

www.mrc-journal.de

**ADVANCED
SCIENCE NEWS**

www.advancedsciencenews.com

{M} acro- molecular

Rapid Communications

www.mrc-journal.de

Table 3. Faradaic impedance data for the magnetic electrode coated with Fe_3O_4-$\gamma Fe_2O_3/(C_{60}Pd_3)_n$ composite and $(C_{60}Pd_3)_n$ polymer.

Potential	R_i [Ω]	C_{dl} [mF]	R_{ct} [Ω]	Y_0	C_L [mF]
Fe_3O_4-$\gamma Fe_2O_3/(C_{60}Pd_3)_n$ composite					
600 mV	125 (1%)	0.051 (8%)	17.2 (12%)	0.33×10^{-2} (15%)	0.637 (4%)
650 mV	131 (1%)	0.072 (6%)	12.5 (15%)	0.36×10^{-2} (28%)	0.554 (3%)
700 mV	132 (1%)	0.090 (9%)	9.2 (27%)	0.39×10^{-2} (22%) 0.42×10^{-2}	0.506 (6%)
750 mV	132 (2%)	0.134 (7%)	4.2 (55%)	0.42×10^{-2} (18%)	0.452 (4%)
$(C_{60}Pd_3)_n$ polymer					
600 mV	112 (13%)	0.004 (5%)	130 (40%)	0.19×10^{-3} (6%)	0.329 (25%)
650 mV	109 (2%)	0.008 (12%)	110 (32%)	0.27×10^{-3} (3%)	0.312 (13%)
700 mV	119 (3%)	0.014 (7%)	75 (24%)	0.47×10^{-3} (3%)	0.506 (25%)
750 mV	105 (3%)	0.029 (7%)	40 (55%)	1.02×10^{-3} (6%)	0.472 (22%)

Both enhancement of electrochemical activity and stability under cyclic charging and discharging are particularly important for application of Fe_3O_4-$\gamma Fe_2O_3/(C_{60}Pd_3)_n$ composite immobilized on the surface of the magnetic electrode in charge storage devices. The results of faradaic impedance measurements indicate that the impedance responses of the electrode coated with the composite are dominated by the capacitance properties of the material. The high electrical capacity of the Fe_3O_4-$\gamma Fe_2O_3/(C_{60}Pd_3)_n$ composite immobilized on the surface of the magnetic electrode and fast charge transfer processes within the composite show that the composite material can act effectively as an electroactive material in electrochemical capacitors. These issues are the subject of ongoing work.

4. Experimental Section

Materials: $FeCl_2 \cdot 4H_2O$, $FeCl_3 \cdot 6H_2O$, 0.5% NH_3 solution, acetone, ethanol, tetra(n-butyl)ammonium hydroxide, $(n$-$C_4H_9)_4NOH$, NaCl, acetonitrile, dichloromethane , and $(n$-$C_4H_9)_4NClO_4$ were used as received for the synthesis of Fe_3O_4 nanoparticles and its composite with $(C_{60}Pd_3)_n$ from Aldrich Chemical Co. Fullerene C_{60} (99%), tris(dibenzylideneacetone) dipalladium(0)-chloroform adduct, $Pd_2(dba)_3 \cdot CHCl_3$, and benzene (99.8%) used for coordination fullerene polymer synthesis were purchased from Aldrich Chemical Co. and used without additional purification. A Milli-Q/Millipore system was used to obtain deionized water with a resistivity of 18.2 MΩ cm.

Instrumentation: Cyclic voltammetry and electrochemical impedance spectroscopy (EIS) experiments were performed using an AUTOLAB (Utrecht, Netherlands) computerized electrochemistry system equipped with a PGSTAT 12 potentiostat and FRA response analyzer expansion cards with a three-electrode cell. The AUTOLAB system was controlled with the GPES 4.9 software provided by the system manufacturer. A silver wire was immersed in an acetonitrile solution of 0.01 M $AgNO_3$ and 0.09 M $(n$-$Bu_4N)ClO_4$ and separated from the substrate electrode by a ceramic frit from Bioanalytical Systems, Inc., which served as the reference electrode. The potential of this electrode is equal to 0.043 V with respect to the ferrocene/ferrocene$^+$ redox couple, which corresponds to 0.725 V with respect to a normal hydrogen electrodFrom a e (NHE). The counter electrode was a platinum tab with an area of ≈0.5 cm².

The design of the working electrode is shown in **Figure 13**. The surface of a gold disc plate served as the working electrode. This gold disc, 2 mm thick and 5 mm in diameter, was immobilized in a Teflon tube. The Teflon tube also contained a neodymium magnet ensuring the deposition of the magnetic material on the outer surface of the gold. The magnet had a remanence of 1290−1320 Tesla and a force of 2.2 kg. The design of the electrode made it possible to remove the magnet from the inside of the Teflon tube when cleaning the electrode. To limit the magnetic deposition of the material on the Teflon surface surrounding the gold disc, an additional Teflon restraint was used. Prior to the electrochemical measurement, this limiting ring was removed from the electrode surface, ensuring that only the gold surface was covered with magnetic material. Prior to the experiments, the electrode was polished with fine Carborundum paper and then with a 0.5-μm alumina slurry. Subsequently, the electrode was sonicated in water to remove traces of alumina from the gold surface, rinsed with water, and dried.

TEM images were obtained using a Tecnai G² 20 X-TWIN microscope (FEI Company, Hillsboro, OR, USA) with a LaB6 emitter and an HAADF detector operating at 200 kV.

SEM experiments were carried out using an INSPECT S50 microscope. The accelerating voltage of the electron beam was 20 keV.

TGA in an atmosphere of purged nitrogen (0.1 dm³ min^{-1}) was performed using a Mettler Toledo Star TGA/DSC system. Two milligrams of sample were weighed, placed in aluminum pans, and heated from 20 °C to 1050 °C at 10 °C min^{-1}.

FT-IR spectra were recorded using a Magna IR 550 Series II spectrometer with a spectral resolution of 4 cm^{-1}.

Powder diffraction studies were carried out using a Supernova diffractometer (Agilent Technologies) operating at 50 kV and 0.8 mA and equipped with a CCD detector and a source: CuKα 1 ($\lambda = 1.54056$ Å). The distance between the sample and detector was 158 cm.

Mössbauer measurements were performed at room temperature using a spectrometer operating in a constant acceleration mode with a ^{57}Co source in Rh matrix. The velocity scale was calibrated using α-Fe standard foil at room temperature.

Synthesis of Magnetic Iron Oxide Particles and $(C_{60}Pd_3)_n$ Nanocomposite: Fe_3O_4-γFe_2O_3 nanoparticles were produced according to the modified synthesis described by Yazadani and Seddigh .[94] At room temperature, 50 mL of 0.1 M Fe^{3+} solution and 25 mL of 0.1 M Fe2+ solution

Figure 12. Nyquist plots of the magnetic electrode coated with a) $(C_{60}Pd_3)_n$ polymer and b) Fe_3O_4-$\gamma Fe_2O_3/(C_{60}Pd_3)_n$ composite formed in 20 mL of benzene containing 0.48×10^{-3} M C_{60}, 0.72×10^{-3} M $Pd_2(dba)_3 \cdot CHCl_3$, and 10 mg Fe_3O_4-γFe_2O_3, at (1) −600, (2) −650, (3) −700, and (4) −750 mV in acetonitrile containing 0.1 M $(n$-$C_4H_9)_4NClO_4$. Marks represent experimental data, and the solid lines present impedance changes for the equivalent circuit. The upper inset in panel a shows the Z''–Z' relationship in the higher frequency range at −700 mV. The lower inset in panel a presents the potential change diagram during faradaic impedance measurements. The inset in panel b shows an equivalent circuit representing the composite/electrolyte interphase.

**ADVANCED
SCIENCE NEWS**

www.advancedsciencenews.com

**[M]acro-molecular
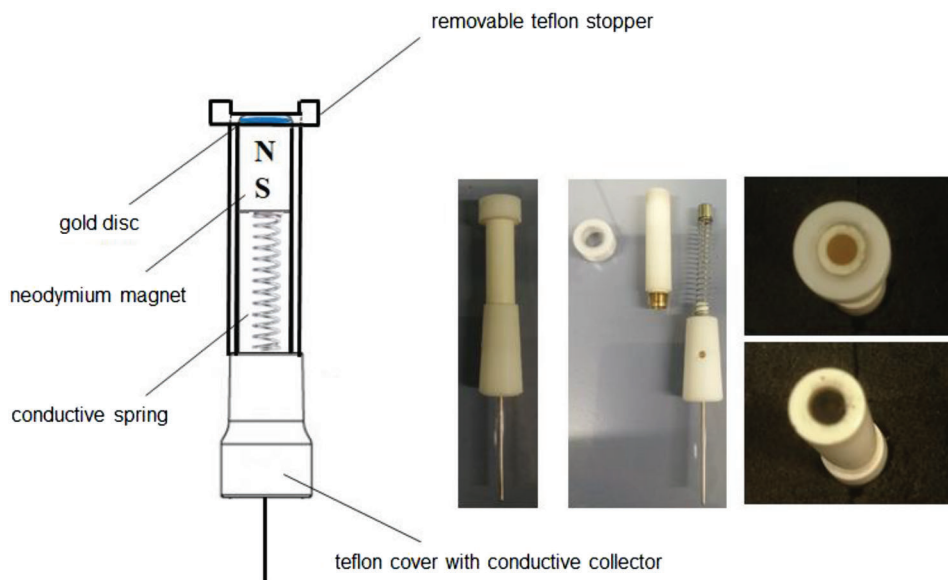Rapid Communications**

www.mrc-journal.de

Figure 13. Schematic illustration of the magnetite electrode and real photo of the test electrode disassembled into parts.

were added to 350 mL of deionized water under an argon atmosphere and vigorously stirred. Next, 35 mL of 1 M NaOH solution was added to the reaction vessel and the mixture was stirred for 3 min. The resultant dark residue was separated from the solution with a permanent magnet. In the last step, the obtained magnetic nanoparticles were washed a few times using deoxygenated deionized water and dried to a powder form in a vacuun oven for 12 h at 80 °C. Due to the possibility of easy oxidation of magnetite nanoparticles to maghemite, in this paper the iron oxide nanoparticle material will be designated as Fe_3O_4-γFe_2O_3.

In the next step, magnetite nanoparticles were dispersed in 10 cm^3 of degassed benzene containing 15 mg of $Pd_2(dba)_3 \cdot CHCl_3$. Next, 10 cm^3 of dissolved benzene containing 7 mg of C_{60} was added. The synthesis was carried out at different times (2–24 h) in an argon atmosphere. Under such conditions, the $(C_{60}Pd_3)_n$ polymer, which exhibits a 3-D structure, was precipitated on the magnetite nanoparticle surface.

Conflict of Interest

The authors declare no conflict of interest.

Data Availability Statement

The data that support the findings of this study are available from the corresponding author upon reasonable request.

[1] C. Li, M. Iqbal, J. Lin, X. Luo, B. Jiang, V. Malgras, K. C.-W. Wu, J. Kim, Y. Yamauchi, *Acc. Chem. Res.* **2018**, *51*, 1764.

[2] P. Bocchetta, D. Frattini, M. Tagliente, F. Selleri, *Curr. Nanosci.* **2020**, *16*, 462.

[3] H.-C. Shin, J. Dong, M. Liu, *Adv. Mater.* **2003**, *15*, 1610.

[4] X. Zhang, K. Wan, P. Subramanian, M. Xu, J. Luo, J. Fransaer, *J. Mater. Chem. A* **2020**, *8*, 7569.

[5] S. Biallozor, A. Kupniewska, *Synth. Met.* **2005**, *155*, 443.

[6] H. Hou, S. Tang, Y. Liu, W. Wang, A. Liang, L. Sun, A. Luo, *J. Electroanal. Chem.* **2022**, *904*, 115921.

[7] A. Kaliyaraj Selva Kumar, Y. Zhang, D. Li, R. G. Compton, *Electrochem. Commun.* **2020**, *121*, 106867.

[8] I. Dumitrescu, P. R. Unwin, J. V. Macpherson, *Chem. Commun.* **2009**, 6886.

[9] E. Asadian, M. Ghalkhani, S. Shahrokhian, *Sens. Actuators, B* **2019**, *293*, 183.

[10] E. Gradzka, K. Winkler, M. Borowska, M. E. Plonska-Brzezinska, L. Echegoyen, *Electrochim. Acta* **2013**, *96*, 274.

[11] M. Deepa, T. K. Saxena, D. P. Singh, K. N. Sood, S. A. Agnihotry, *Electrochim. Acta* **2006**, *51*, 1974.

[12] M. M. Collinson, *Acc. Chem. Res.* **2007**, *40*, 777.

[13] L. Ye, K. Wen, Z. Zhang, F. Yang, Y. Liang, W. Lv, Y. Lin, J. Gu, J. H. Dickerson, W. He, W. He, *Adv. Energy Mater.* **2016**, *6*, 1502018.

[14] L. Cordero-Arias, S. Cabanas-Polo, J. Gilabert, O. M. Goudouri, E. Sanchez, S. Virtanen, A. R. Boccaccini, *Adv. Appl. Ceram.* **2014**, *113*, 42.

[15] M. Diba, A. García-Gallastegui, R. N. Klupp Taylor, F. Pishbin, M. P. Ryan, M. S. P. Shaffer, A. R. Boccaccini, *Carbon* **2014**, *67*, 656.

[16] M. Wang, L. D. Duong, J. S. Oh, N. T. Mai, S. Kim, S. Hong, J. D. Nam, *ACS Appl. Mater. Interfaces* **2014**, *6*, 1747.

[17] W. Kutner, P. Pieta, R. Nowakowski, J. W. Sobczak, Z. Kaszkur, A. L. Mccarty, F. D'souza, *Chem. Mater.* **2005**, *17*, 5635.

ADVANCED
SCIENCE NEWS

www.advancedsciencenews.com

acro-
Molecular
Rapid Communications

www.mrc-journal.de

[18] C. N. Sayre, D. M. Collard, *Langmuir* **1997**, *13*, 714.

[19] M. Mazur, P. Krysinski, B. Palys, *J. Electroanal. Chem.* **2002**, *533*, 145.

[20] E. Ruckenstein, Z. F. Li, *Adv. Colloid Interface Sci.* **2005**, *113*, 43.

[21] D. Zhao, X. Guo, Y. Gao, F. Gao, *ACS Appl. Mater. Interfaces* **2012**, *4*, 5583.

[22] C. Peng, S. Zhang, D. Jewell, G. Z. Chen, *Prog. Nat. Sci.* **2008**, *18*, 777.

[23] J. Wang, J. Wang, Z. Kong, K. Lv, C. Teng, Y. Zhu, *Adv. Mater.* **2017**, *29*, 1703044.

[24] A. Kumar, H. K. Rathore, D. Sarkar, A. Shukla, *Electrochem. Sci. Adv.* **2022**, *2*, e2100187.

[25] M. A. A. Mohd Abdah, N. H. N. Azman, S. Kulandaivalu, Y. Sulaiman, *Mater. Des.* **2020**, *186*, 108199.

[26] K. R. Reddy, B. C. Sin, K. S. Ryu, J.-C. Kim, H. Chung, Y. Lee, *Synth. Met.* **2009**, *159*, 595.

[27] N. K., C. S. Rout, *RSC Adv.* **2021**, *11*, 5659.

[28] J. Mürbe, A. Rechtenbach, J. Töpfer, *Mater. Chem. Phys.* **2008**, *110*, 426.

[29] Y. Zhang, S. Xu, Y. Luo, S. Pan, H. Ding, G. Li, *J. Mater. Chem.* **2011**, *21*, 3664.

[30] G. Zhao, J.-J. Feng, Q.-L. Zhang, S.-P. Li, H.-Y. Chen, *Chem. Mater.* **2005**, *17*, 3154.

[31] A. Cotar, A. Grumezescu, K. C. Huang, G. Voicu, M. Chifiriue, R. Radulescu, *Biointerface Res. Appl. Chem.* **2013**, *3*, 559.

[32] R. Acharya, K. Parida, *Biointerface Res. Appl. Chem.* **2020**, *10*, 5266.

[33] T. Gu, Y. Zhang, S. A. Khan, T. A. Hatton, *Colloid Interface Sci. Commun.* **2019**, *28*, 1.

[34] M. C. Menard, K. J. Takeuchi, A. C. Marschilok, E. S. Takeuchi, *Phys. Chem. Chem. Phys.* **2013**, *15*, 18539.

[35] S. D. A. Zaidi, C. Wang, B. György, C. Sun, H. Yuan, L. Tian, J. Chen, *J. Colloid Interface Sci.* **2020**, *569*, 164.

[36] A. Cotar, A. Grumezescu, K. C. Huang, G. Voicu, M. Chifiriuc, R. Radulescu, *Biointerface Res. Appl. Chem.* **2013**, *3*, 559.

[37] T. Radu, A. Petran, D. Olteanu, I. Baldea, M. Potara, R. Turcu, *Appl. Surf. Sci.* **2020**, *501*, 144267.

[38] L. Y. Novoselova, *Appl. Surf. Sci.* **2021**, *539*, 148275.

[39] J. Winsett, A. Moilanen, K. Paudel, S. Kamali, K. Ding, W. Cribb, D. Seifu, S. Neupane, *SN Appl. Sci.* **2019**, *1*, 1636.

[40] I. S. Unver, Z. Durmus, *IEEE Trans. Magn.* **2017**, *53*, 2001708.

[41] M. L. M. Elizalde, C. Acha, M. S. Moreno, P. S. Antonel, *J. Mater. Chem. C* **2022**, *10*, 18264.

[42] M. Kryszewski, J. K. Jeszka, *Synth. Met.* **1998**, *94*, 99.

[43] K. Minnici, Y. H. Kwon, L. M. Housel, G. D. Renderos, J. F. Ponder, C. Buckley, J. R. Reynolds, K. J. Takeuchi, E. S. Takeuchi, A. C. Marschilok, E. Reichmanis, *ACS Appl. Energy Mater.* **2019**, *2*, 7584.

[44] J. H. Kim, F. F. Fang, H. J. Choi, Y. Seo, *Mater. Lett.* **2008**, *62*, 2897.

[45] B. Belaabed, J. L. Wojkiewicz, S. Lamouri, N. El Kamchi, T. Lasri, *J. Alloys Compd.* **2012**, *527*, 137.

[46] G. Bencsik, C. Janáky, B. Endrodi, C. Visy, *Electrochim. Acta* **2012**, *73*, 53.

[47] C. Janáky, B. Endrodi, O. Berkesi, C. Visy, *J. Phys. Chem. C* **2010**, *114*, 19338.

[48] S. P. Pawar, G. Melo, U. Sundararaj, *Compos. Sci. Technol.* **2019**, *183*, 107802.

[49] V. D. Nithya, N. Sabari Arul, *J. Mater. Chem. A* **2016**, *4*, 10767.

[50] X. Zhao, C. Johnston, A. Crossley, P. S. Grant, *J. Mater. Chem.* **2010**, *20*, 7637.

[51] F. Xu, L. Ma, Q. Huo, M. Gan, J. Tang, *J. Magn. Magn. Mater.* **2015**, *374*, 311.

[52] A. C. V. De Araújo, R. J. De Oliveira, S. Alves Júnior, A. R. Rodrigues, F. L. A. Machado, F. A. O. Cabral, W. M. De Azevedo, *Synth. Met.* **2010**, *160*, 685.

[53] B. E. Jaramillo-Tabares, F. J. Isaza, S. I. C. D. Torresi, *Mater. Chem. Phys.* **2012**, *132*, 529.

[54] D. Donescu, R. C. Fierascu, M. Ghiurea, D. Manaila-Maximean, C. A. Nicolae, R. Somoghi, C. I. Spataru, N. Stanica, V. Raditoiu, E. Vasile, *Appl. Surf. Sci.* **2017**, *414*, 8.

[55] M. D. Butterworth, S. A. Bell, S. P. Armes, A. W. Simpson, *J. Colloid Interface Sci.* **1996**, *183*, 91.

[56] D. E. Park, H. S. Chae, H. J. Choi, A. Maity, *J. Mater. Chem. C* **2015**, *3*, 3150.

[57] K.-M. Mangold, J. Schuster, C. Weidlich, *Electrochim. Acta* **2011**, *56*, 3616.

[58] S.-J. Yen, E.-C. Chen, R.-K. Chiang, T.-M. Wu, *J. Polym. Sci., Part B: Polym. Phys.* **2008**, *46*, 1291.

[59] B. Singh, R.-A. Doong, D. S. Chauhan, A. K. Dubey, Anshumali, *Mater. Chem. Phys.* **2018**, *205*, 462.

[60] F. Entezari Juybari, A. Kamran-Pirzaman, M. Ghorbani, *Inorg. Nano-Met. Chem.* **2017**, *47*, 121.

[61] W. Ceunen, A. Van Oosten, R. Vleugels, J. De Winter, P. Gerbaux, Z. Li, S. De Feyter, G. Koeckelberghs, *Polym. Chem.* **2018**, *9*, 3029.

[62] R. C. Haddon, *Philos. Trans. R. Soc., A* **1993**, *343*, 53.

[63] Q. Xie, E. Perez-Cordero, L. Echegoyen, *J. Am. Chem. Soc.* **1992**, *114*, 3978.

[64] C. A. Reed, R. D. Bolskar, *Chem. Rev.* **2000**, *100*, 1075.

[65] F. Giacalone, N. Martín, *Chem. Rev.* **2006**, *106*, 5136.

[66] F. Giacalone, N. Martín, *Adv. Mater.* **2010**, *22*, 4220.

[67] C. Bruno, M. Marcaccio, D. Paolucci, C. Castellarin-Cudia, A. Goldoni, A. V. Streletskii, T. Drewello, S. Barison, A. Venturini, F. Zerbetto, F. Paolucci, *J. Am. Chem. Soc.* **2008**, *130*, 3788.

[68] K. Winkler, A. L. Balch, *C. R. Chimie* **2006**, *9*, 928.

[69] K. Winkler, A. L. Balch, W. Kutner, *J. Solid State Electrochem.* **2006**, *10*, 761.

[70] J. R. Winkler, H. B. Gray, *Chem. Rev.* **2016**, *116*, 8313.

[71] E. Gradzka, M. Wysocka-Zolopa, K. Winkler, *Adv. Energy Mater.* **2020**, *10*, 2001443.

[72] K. Winkler, A. L. Balch, *Coord. Chem. Rev.* **2021**, *438*, 213623.

[73] H. Nagashima, A. Nakaoka, Y. Saito, M. Kato, T. Kawanishi, K. Itoh, *J. Chem. Soc., Chem. Commun.* **1992**, 377.

[74] A. L. Balch, D. A. Costa, K. Winkler, *J. Am. Chem. Soc.* **1998**, *120*, 9614.

[75] K. Winkler, K. Noworyta, W. Kutner, A. L. Balch, *J. Electrochem. Soc.* **2000**, *147*, 2597.

[76] E. Brancewicz, E. Gradzka, A. Basa, K. Winkler, *Electrochim. Acta* **2014**, *128*, 91.

[77] K. Winkler, A. De Bettencourt-Dias, A. L. Balch, *Chem. Mater.* **2000**, *12*, 1386.

[78] K. Winkler, A. De Bettencourt-Dias, A. L. Balch, *Chem. Mater.* **1999**, *11*, 2265.

[79] K. Winkler, E. Grodzka, F. D'souza, A. L. Balch, *J. Electrochem. Soc.* **2007**, *154*, K1.

[80] E. Brancewicz, E. Gradzka, K. Winkler, *J. Solid State Electrochem.* **2013**, *17*, 1233.

[81] E. Gradzka, M. Wysocka-Zolopa, K. Winkler, *J. Phys. Chem. C* **2014**, *118*, 14061.

[82] J. Goclon, K. Winkler, J. T. Margraf, *RSC Adv.* **2017**, *7*, 2202.

[83] E. Grodzka, P. Pieta, P. Dluzewski, W. Kutner, K. Winkler, *Electrochim. Acta* **2009**, *54*, 5621.

[84] P. Pieta, E. Grodzka, K. Winkler, G. M. Venukadasula, F. D'souza, W. Kutner, *Phys. Status Solidi B* **2008**, *245*, 2292.

[85] P. Pieta, E. Grodzka, K. Winkler, M. Warczak, A. Sadkowski, G. Z. Zukowska, G. M. Venukadasula, F. D'souza, W. Kutner, *J. Phys. Chem. B* **2009**, *113*, 6682.

[86] E. Gradzka, E. Brancewicz, K. Winkler, *ECS J. Solid State Sci. Technol.* **2013**, *2*, M3151.

[87] A. V. Talyzin, A. Dzwilewski, M. Pudelko, *Carbon* **2007**, *45*, 2564.

ADVANCED
SCIENCE NEWS

www.advancedsciencenews.com

macro-
Molecular
Rapid Communications

www.mrc-journal.de

[88] R. M. Cornell, U. Schwertmann, *The Iron Oxides: Structure, Properties, Reactions, Occurrences and Uses*, 2nd ed., Wiley-VCH, Weinheim, Germany, **2003**.

[89] M. R. Zachariah, M. I. Aquino, R. D. Shull, E. B. Steel, *Nanostruct. Mater.* **1995**, *5*, 383.

[90] Ö. Helgason, H. K. Rasmussen, S. Mørup, *J. Magn. Magn. Mater.* **2006**, *302*, 413.

[91] E. Tronc, D. Fiorani, M. Noguès, A. M. Testa, F. Lucari, F. D'orazio, J. M. Grenèche, W. Wernsdorfer, N. Galvez, C. Chanéac, D. Mailly, J. P. Jolivet, *J. Magn. Magn. Mater.* **2003**, *262*, 6.

[92] L. Nalbandian, E. Patrikiadou, V. Zaspalis, A. Patrikidou, E. Hatzidaki, C. N. Papandreou, *Curr. Nanosci.* **2016**, *12*, 455.

[93] V. N. Ivanova, *J. Struct. Chem.* **2000**, *41*, 135.

[94] F. Yazdani, M. Seddigh, *Mater. Chem. Phys.* **2016**, *184*, 318.